Supporting Information

Assembling highly efficient X-ray and UV-visible light detectors using a VS_2–MoS_2 and VS_2–WS_2 hybrid composite-embedded perovskite layer

Dhanasekaran Vikraman[a], Hailiang Liu[b], Syed Hassan Abbas Jaffery[c,d], Sajjad Hussain[c,d], K. Karuppasamy[e,f], Duhee Lee[a], Jungwon Kang[b], Jongwan Jung[c,d], Hyun-Seok Kim[a*]

[a] Division of Electronics and Electrical Engineering, Dongguk University-Seoul, Seoul 04620, Republic of Korea.
[b] Convergence Semiconductor Research Center, Department of Electronics and Electrical Engineering, Dankook University, Yongin 16890, Republic of Korea.
[c] Hybrid Materials Center (HMC), Sejong University, Seoul 05006, Republic of Korea.
[d] Department of Nanotechnology and Advanced Materials Engineering, Sejong University, Seoul 05006, Republic of Korea.
[e] Department of Chemical and Petroleum Engineering, Khalifa University of Science and Technology, Abu Dhabi, 127788, United Arab Emirates
[f] Emirates Nuclear Technology Center (ENTC), Khalifa University of Science and Technology, Abu Dhabi, 127788, United Arab Emirates
* Corresponding author's Email: hyunseokk@dongguk.edu

S1. Synthesis of MoS_2, WS_2 and VS_2

Simple hydrothermal process was utilized to assemble the MoS_2 nanostructures. The precursors, 0.2 g of ammonium molybdate ($(NH_4)_6Mo_7O_{24}\cdot 4H_2O$) and 1.15 g thiourea ($CH_4N_2S$) were dissolved in the 25 mL deionized water (DI), then blended under continuous stirring until transformed as a transparent solution. Subsequently, as prepared solution was transferred into 100 mL Teflon-lined stainless steel autoclave, heated at 220 °C for 20 h. After cooling naturally to room temperature, the product was flushed with DI and ethanol for several times and dried at 80 °C in vacuum for 12 h.

For WS_2 growth, 0.2 g of ammonium tungsten oxide hydrate $(NH_4)_6H_2W_{12}O_{40}\cdot xH_2O$) and 1.15 g of CH_4N_2S were dissolved in 25 ml of DI separately, then mixed under vigorous stirring to form a homogeneous solution. Meanwhile, oxalic acid dihydrate ($H_2C_2O_4\cdot 2H_2O$)

was added to the above solution as the catalyst with the pH adjusted at 2. As prepared solution was transferred into a 100 ml Teflon-lined stainless steel autoclave, reaction temperature fixed at 220 °C for 24 h, then naturally cooled down to room temperature. The above procedure was followed to clean and dry the nanopowders.

For VS_2 growth, 0.2 g of ammonium vanadate (NH_4VO_3) and 1.15 g of CH_4N_2S were dissolved in 2 ml of DI separately, then mixed under vigorous stirring to form a homogeneous solution. At the same time 2 ml ammonia water ($NH_3.H_2O$) was added slowly dropwise to get the uniform solution. After 60min vigorous stirring, the solution was placed in 100ml stainless steel lined Teflon auto-clave with temperature fixed at 220 °C for 24 h. The above procedure was followed to clean and dry the nanopowders.

S2. Characterization

The electronic configuration of nanostructures was characterized by Raman spectroscope (Renishaw inVia RE04). Energy dispersive analysis combined JEOL JSM-6700F field emission scanning electron microscopy was used to analyze the morphological and compositional properties of synthesized hybrid nanostructures. X-ray photoelectron spectroscopy analysis was performed using PHI 5000 Versa Probe equipped with a monochromatic Al Kα radiation source (25W, 6.7×10^{-8} Pa). The surface topography of prepared active layers was measured using atomic force microscopy (Park Systems XE-150) operating in non-contact mode with 3 μm × 3 μm scan size. UV-vis optical spectroscopy (Optizen 2120UV) was used to measure the absorption spectra of active layer. Electrochemical impedance profiles were recorded using the PARSTAT 1000, PAR, USA.

To convert incident X-ray photons into visible photons, the proposed detector was joined with CsI (Tl) scintillators (Hamamatsu J13113) and the generated charge carriers during exposure were measured with the electrometer. The scintillator-coupled detector J-V

characteristics were recorded using an X-ray generator (AJEX 2000H). The distance between the X-ray source and the scintillator-coupled detector was about 30 cm, and the exposed X-ray dose was measured using an ion chamber (Capintec CII50) at the same distance. The constant 3.44 mGy of dose rate and -0.6 V of applied bias voltage for X-ray source were used for the all the measurement. To tune the charge-carrier collection, the bias voltage to the detector from -0.2 to -1.0V and dose rate from 1.19 to 5.56 mGy were applied. The operating conditions of X-ray generator were fixed at 1.57 sec, 80 kVp and 63 mAÂus for X-ray exposure time, tube voltage and tube current, respectively for all the experiments. The collected current density (CCD) during the X-ray irradiation on-condition and the dark current density (DCD) during the X-ray irradiation off-condition were calculated by Equations (1), and (2), respectively. The sensitivity was calculated using Equation (3), which represented the generated current in proportion to the absorbed dose.

$$CCD\left[\mu A/cm^2\right] = \frac{Collected\ Current\ during\ X-ray\ ON}{Exposed\ Detection\ Area} \quad (1)$$

$$DCD\left[\mu A/cm^2\right] = \frac{Collected\ Current\ during\ X-ray\ OFF}{Exposed\ Detection\ Area} \quad (2)$$

$$Sensitivity\left[\mu A/mGy\cdot cm^2\right] = \frac{CCD-DCD}{Absorbed\ Dose} \quad (3)$$

The absorbed dose from X-ray exposure was measured using an ion chamber.

The photodetector characteristics of prepared heterojunction devices were accomplished using a continuous wave laser beam with the different wavelength light source (365-740 nm) which was directly illumined on the device. The electrical outcomes were recorded at room temperature using a Keithley 4200A-SCS analyzer.

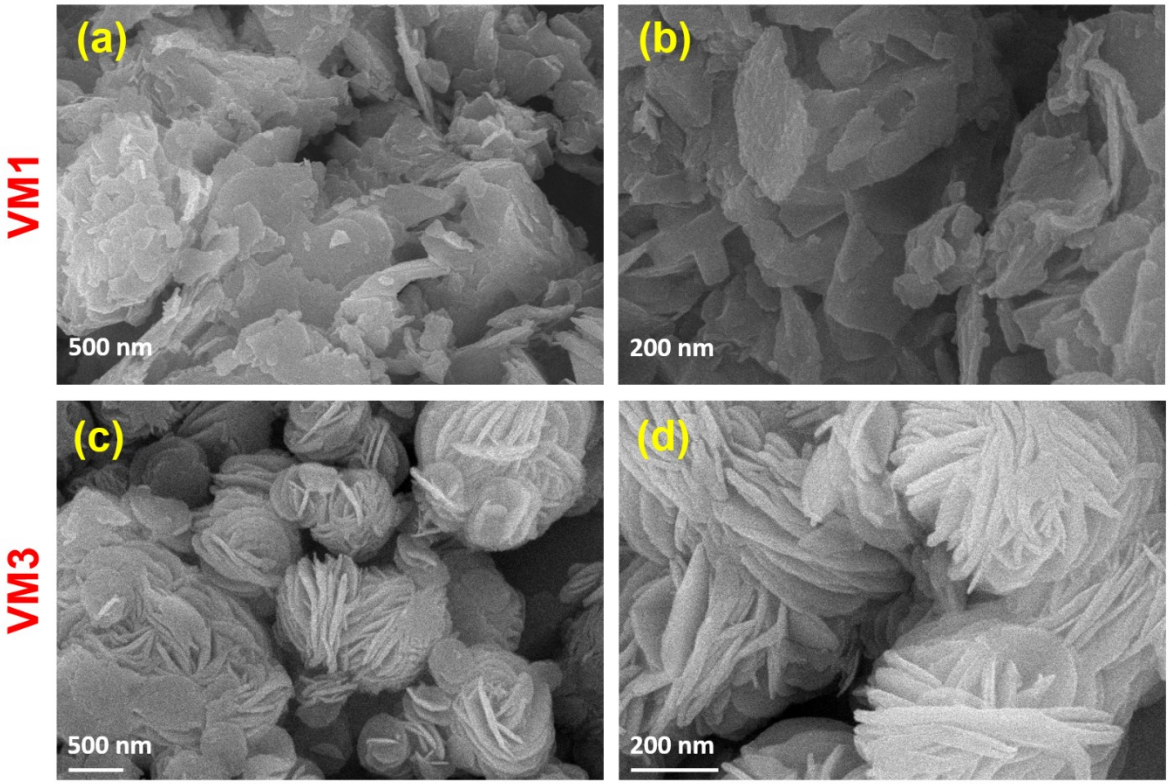

Figure S1. FESEM micrographs of (a-b) VM1 and (c-d) VM3 nanostructures

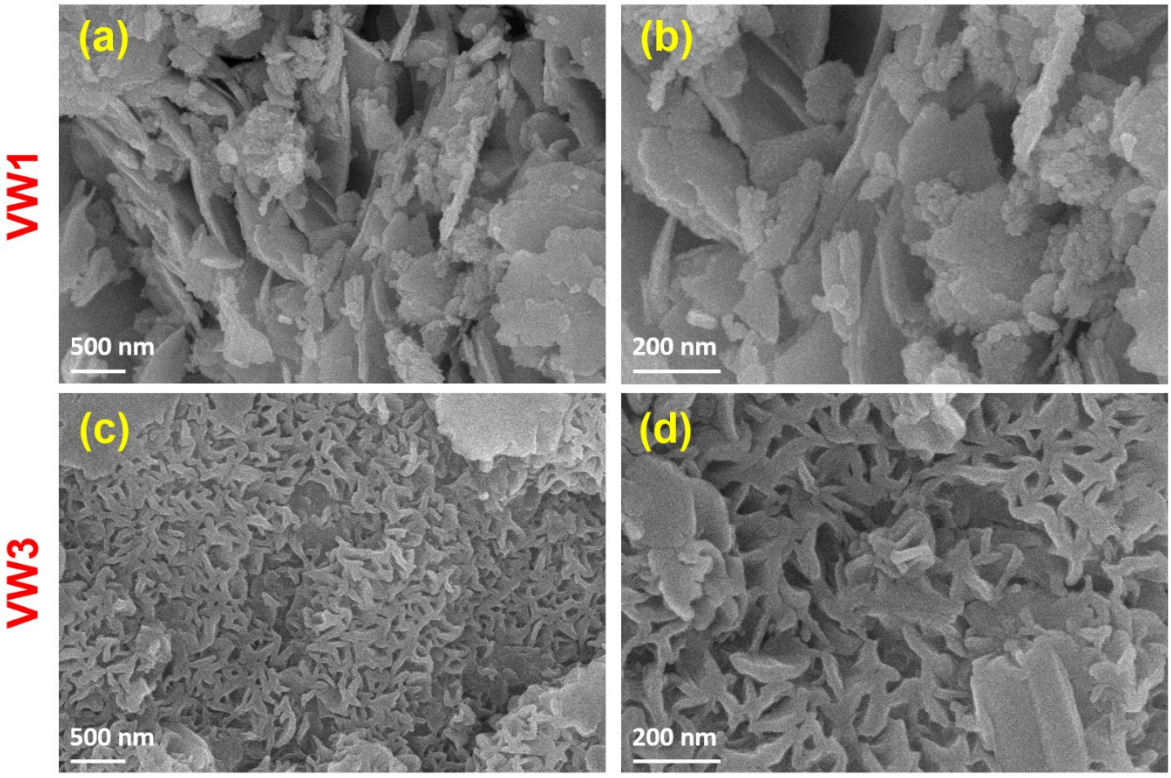

Figure S2. FESEM micrographs of (a-b) VW1 and (c-d) VW3 nanostructures

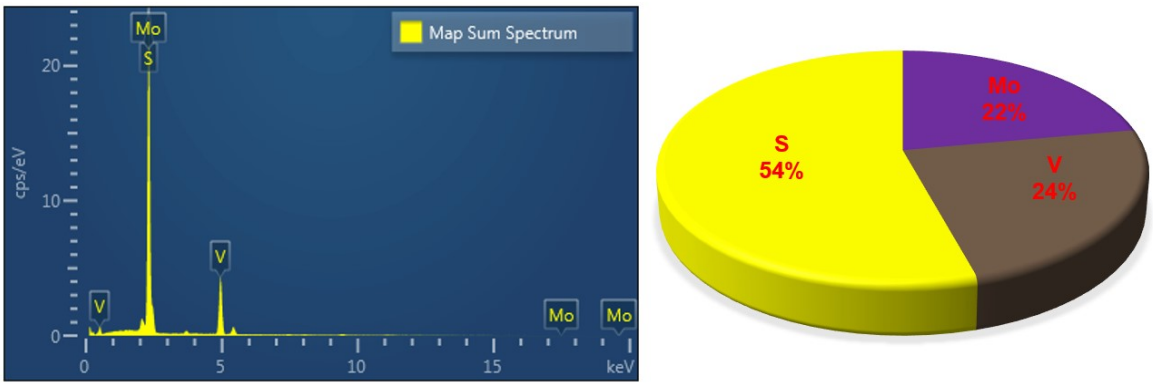

Figure S3. EDX profile of VM2 hybrid nanostructures.

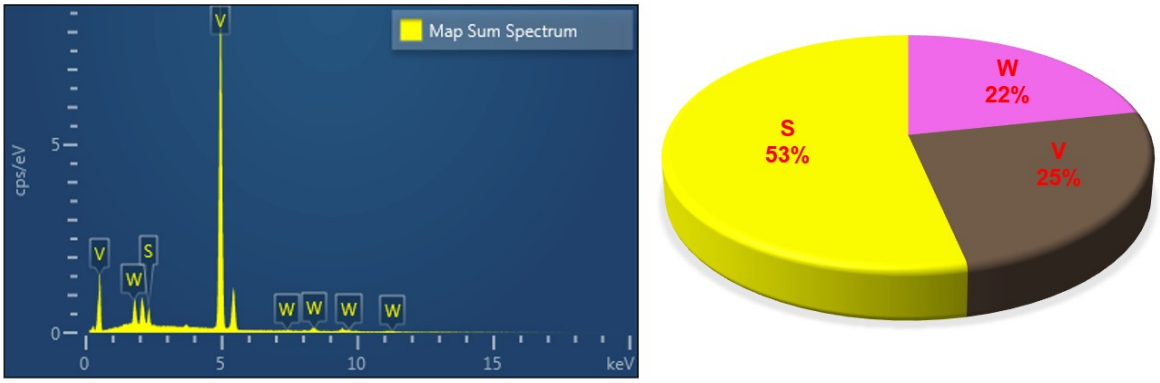

Figure S4. EDX profile of VW2 hybrid nanostructures.

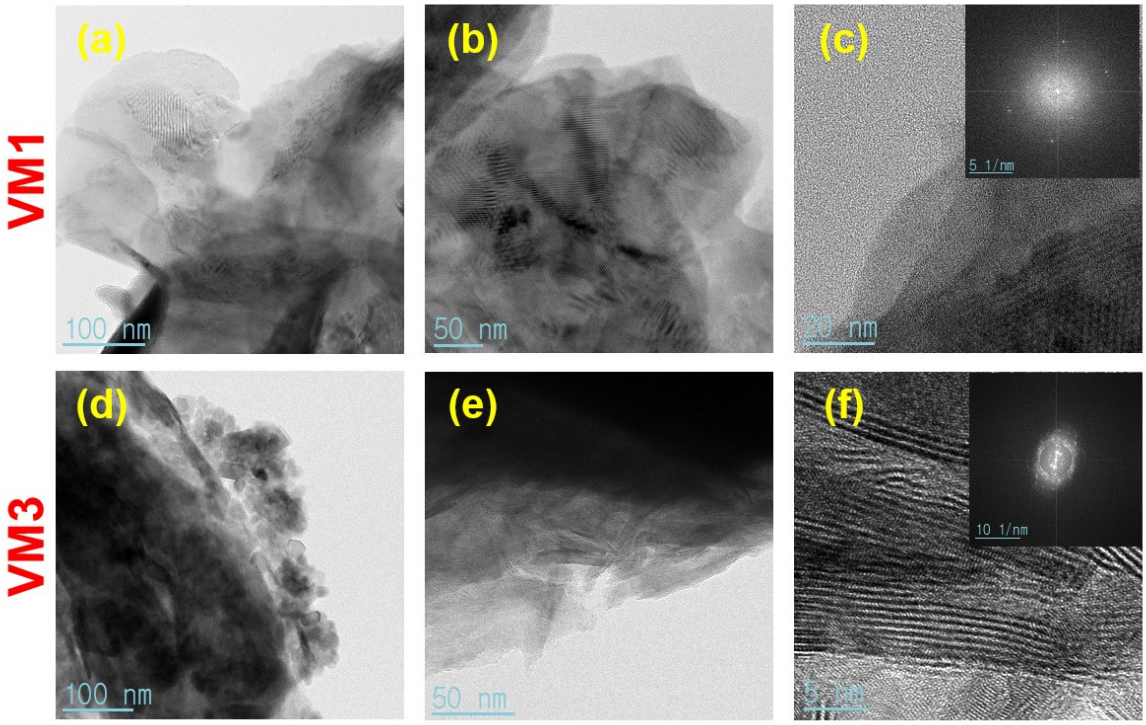

Figure S5. TEM micrographs of (a-c) VM1 and (d-f) VM3 nanostructures.

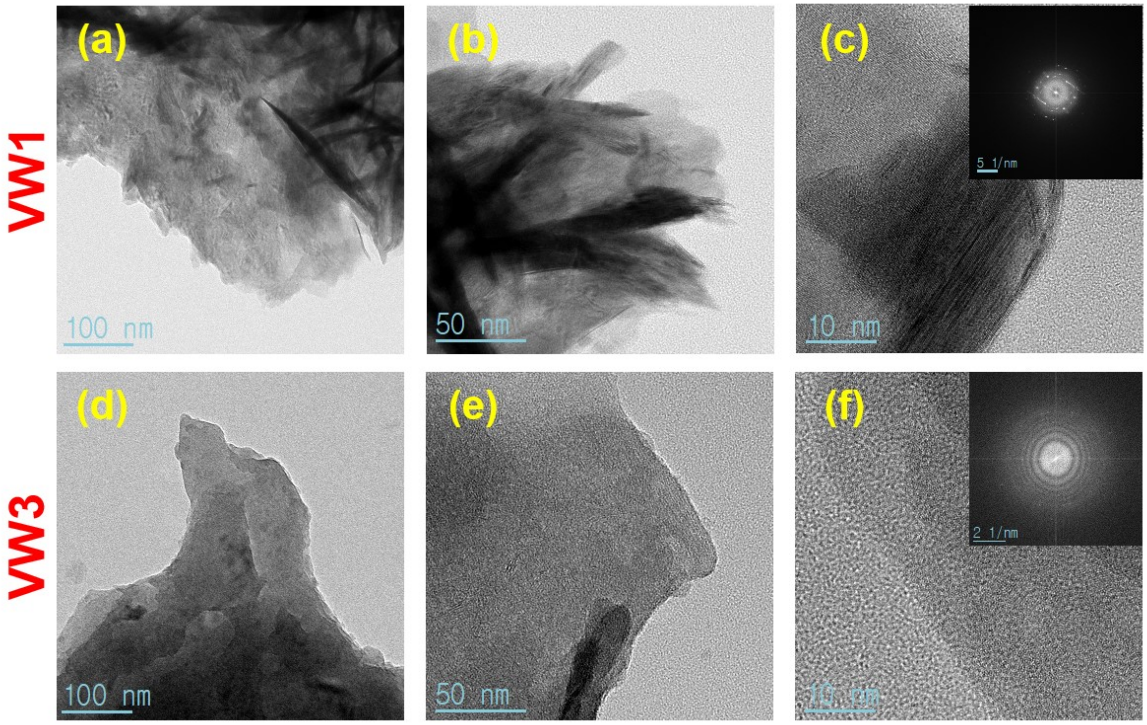

Figure S6. TEM micrographs of (a-c) VW1 and (d-f) VW3 nanostructures.

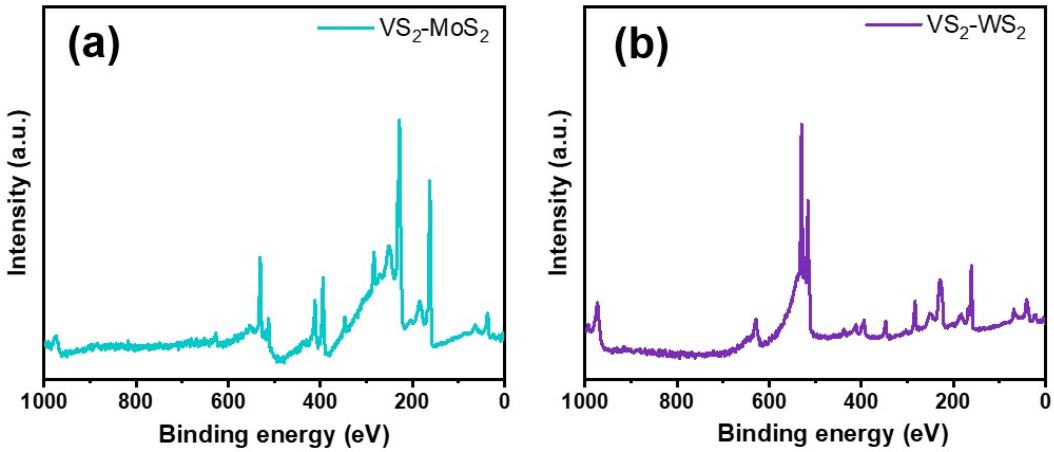

Figure S7. XPS survey spectra of (a) VM2 and (b) VW2 hybrid-structures.

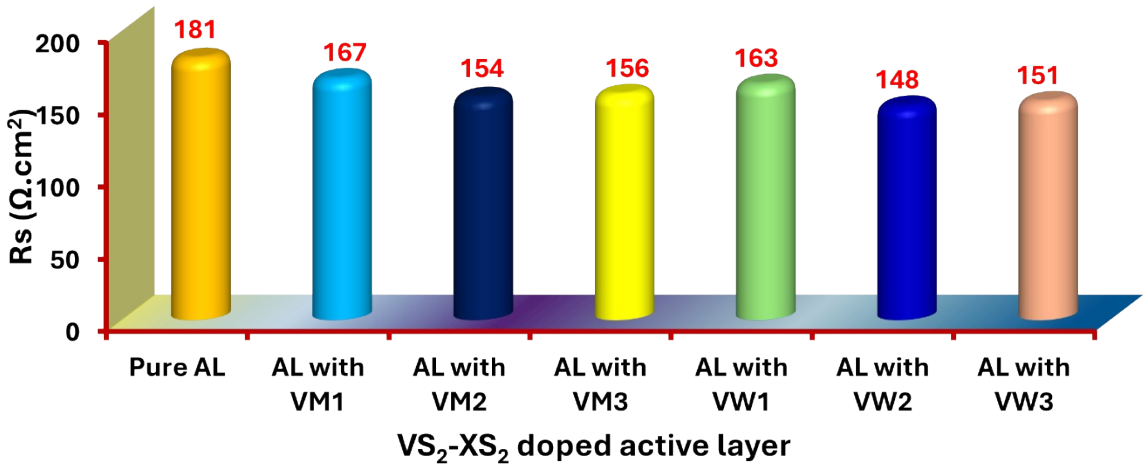

Figure S8. Resistivity of pure and VM1-, VM2-, VM3-, VW1-, VW2-, and VW3-doped $Cs_{0.1}MA_{0.9}PbI_3$ active layer composed device

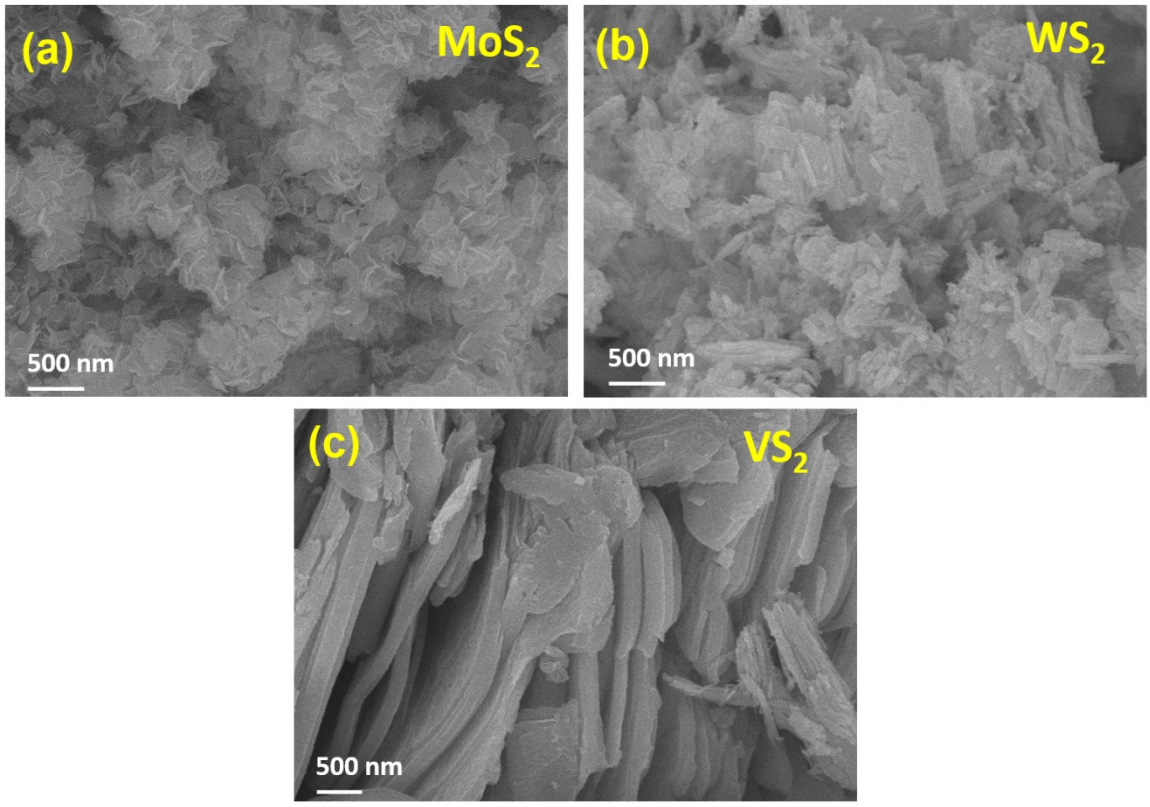

Figure S9. FESEM images of (a) MoS_2, (b) VS_2 and (c) WS_2 nano-structures.

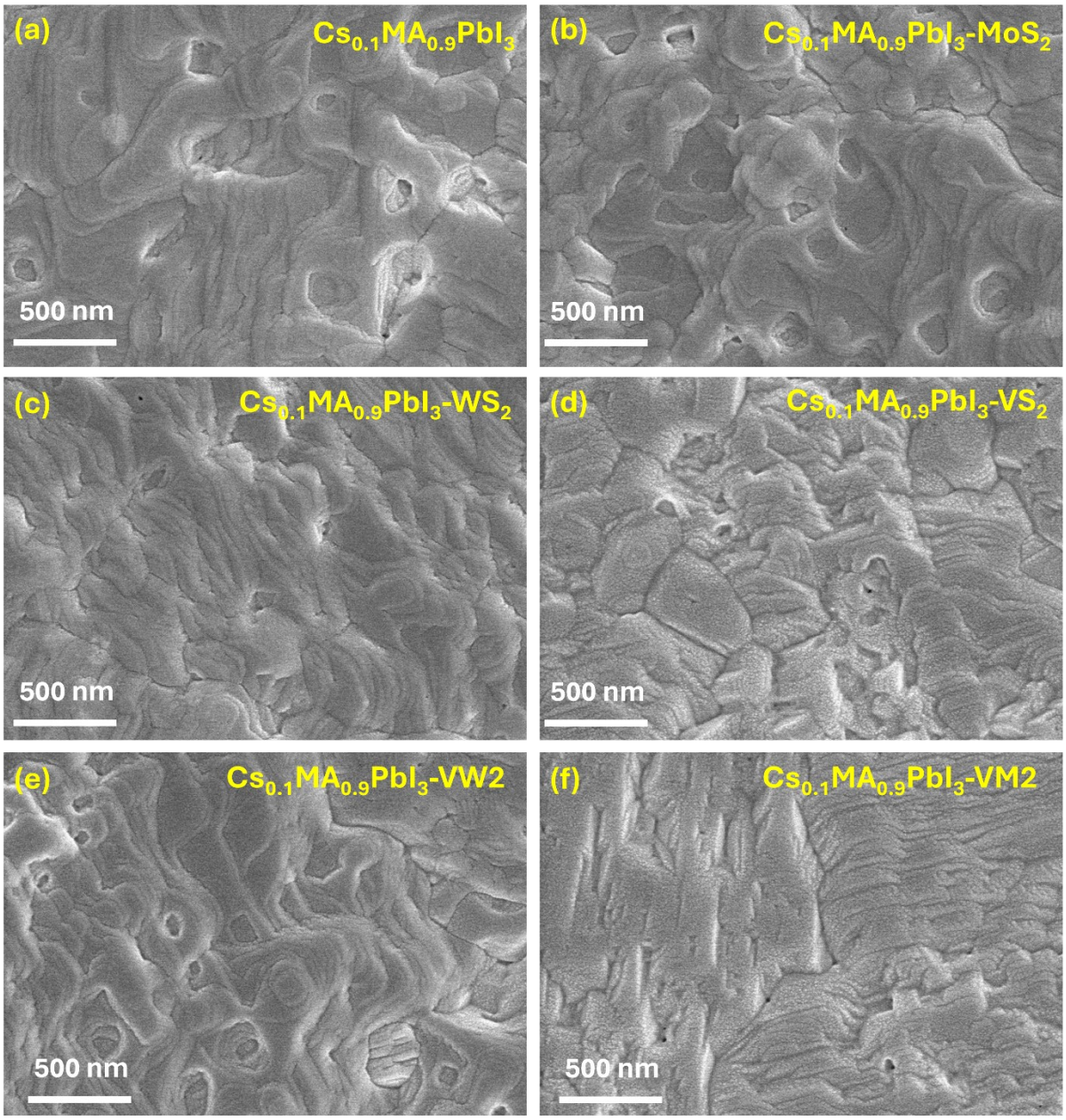

Figure S10. FESEM images of (a) pristine and MoS_2-, WS_2-, VS_2-, VW2-, and VM2-doped active layers

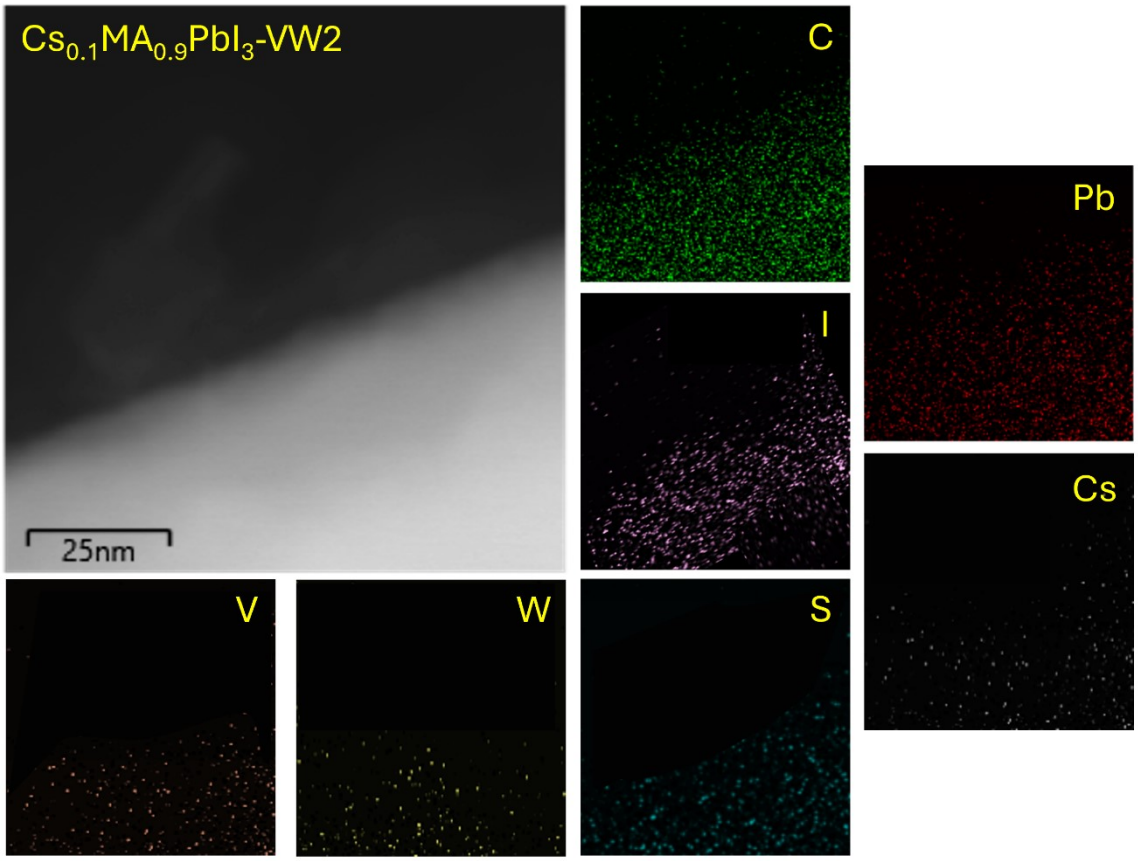

Figure S11. TEM elemental mapping distribution image of VW2-doped active layer and their C, I, V, W, S, Pb and Cs elements dispersion.

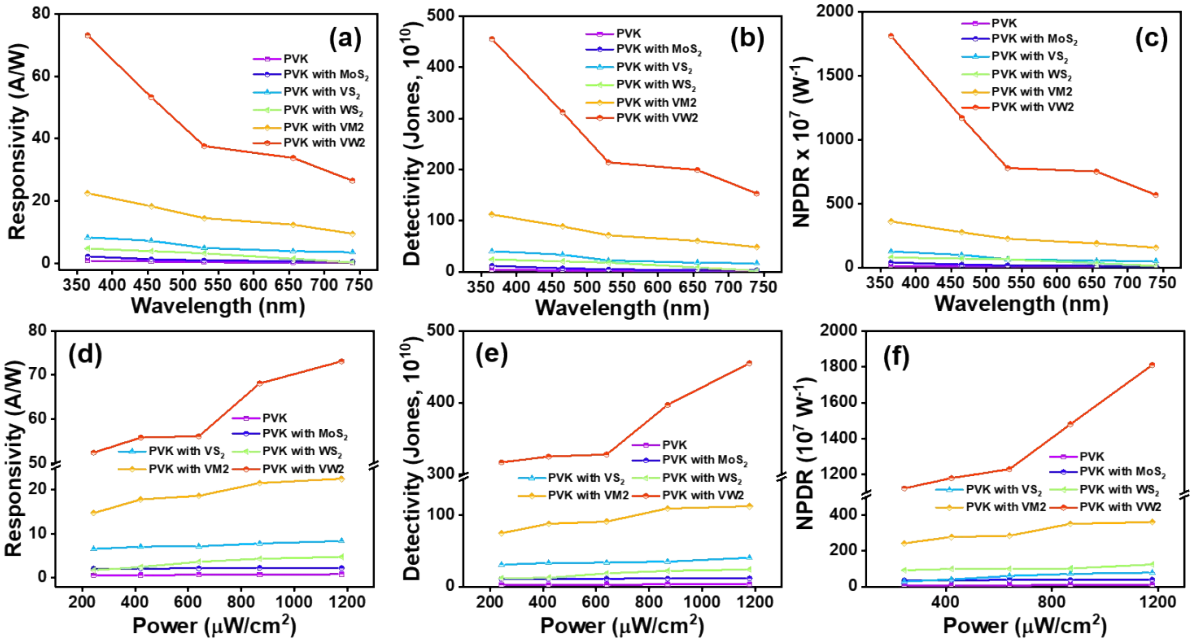

Figure S12. (a) Responsivity, (b) detectivity, and (c) NPDR variations under laser illumination of different wavelengths at a constant power of 1179 μW/cm^2; (d) responsivity, (e) detectivity, and (f) NPDR variations under illumination with different laser powers at a constant wavelength of 365 nm for the pristine and MoS_2, VS_2, WS_2, VM2 VS_2–MoS_2, and VW2 VS_2–WS_2-doped perovskite layer.

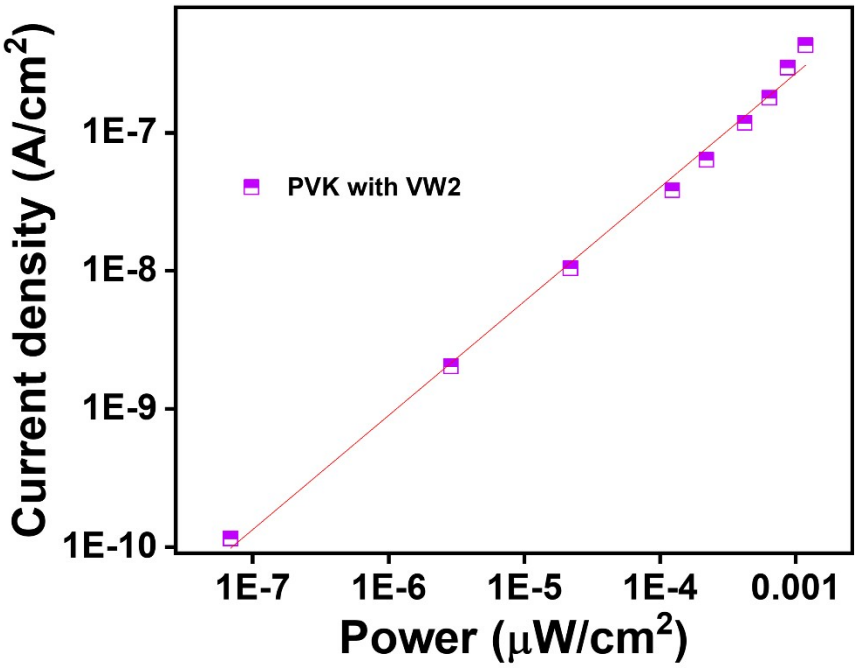

Figure S13. LDR profile of VW2 VS_2–WS_2-doped perovskite layer composed device.

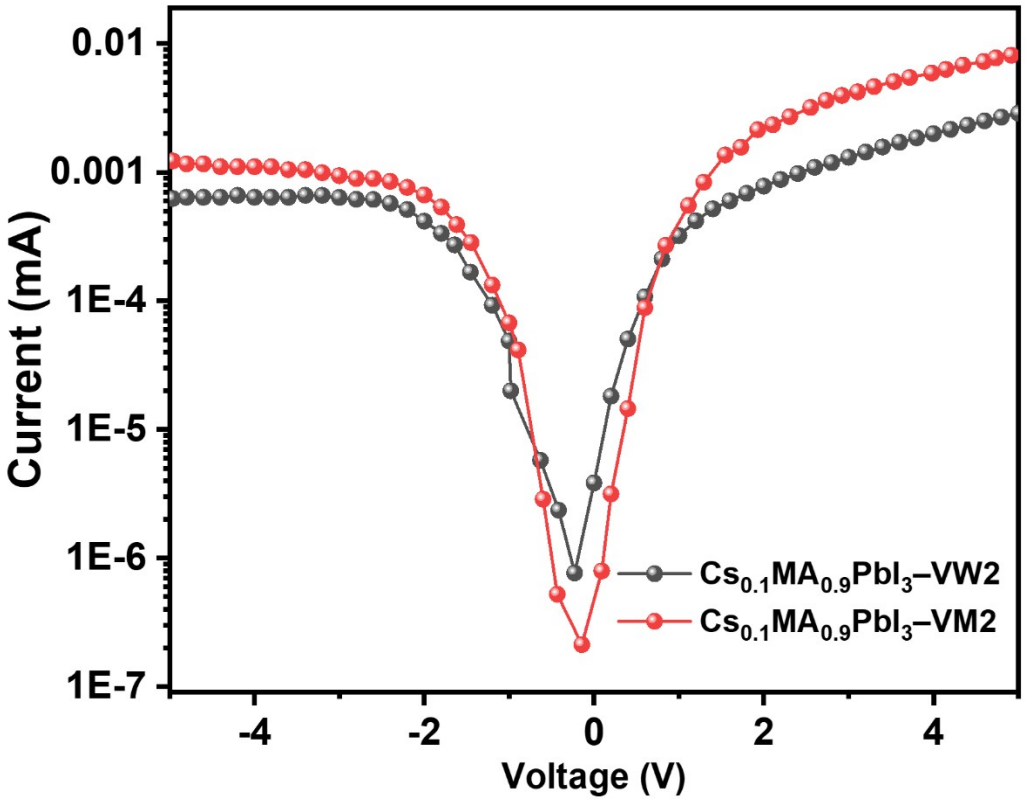

Figure S14. J-V profiles for the VW2 and VM2 doped perovskite layer photodetector

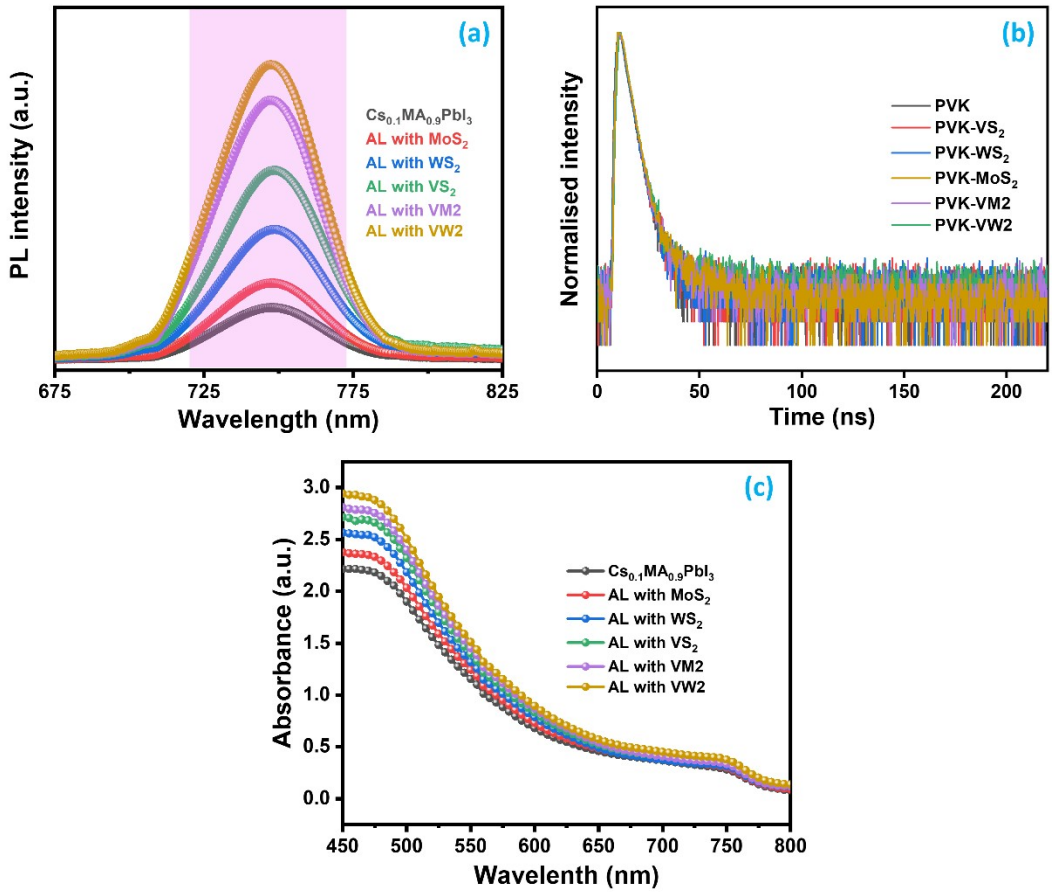

Figure S15. (a) PL, (b) TRPL and (c) UV–Vis–NIR absorption spectra for the $Cs_{0.1}MA_{0.9}PbI_3$doped with pristine and MoS_2, VS_2, WS_2 and VS_2–XS_2 hybrids.

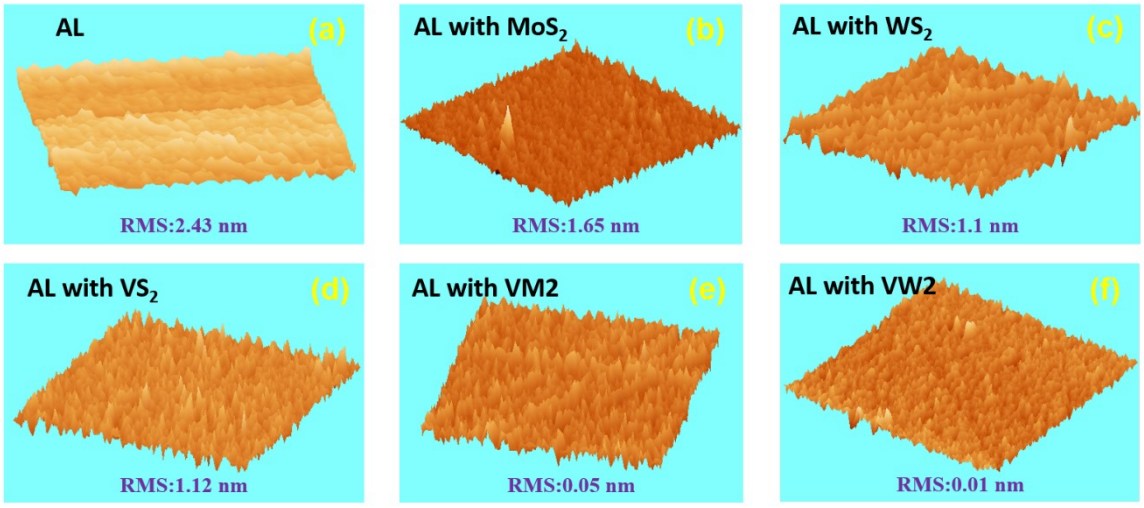

Figure S16. AFM images of (a) pure and (b) MoS_2, (c) WS_2, (d) VS_2, (e) VM2, and (f) VW2 doped (10 vol.%) $Cs_{0.1}MA_{0.9}PbI_3$ perovskite layer.

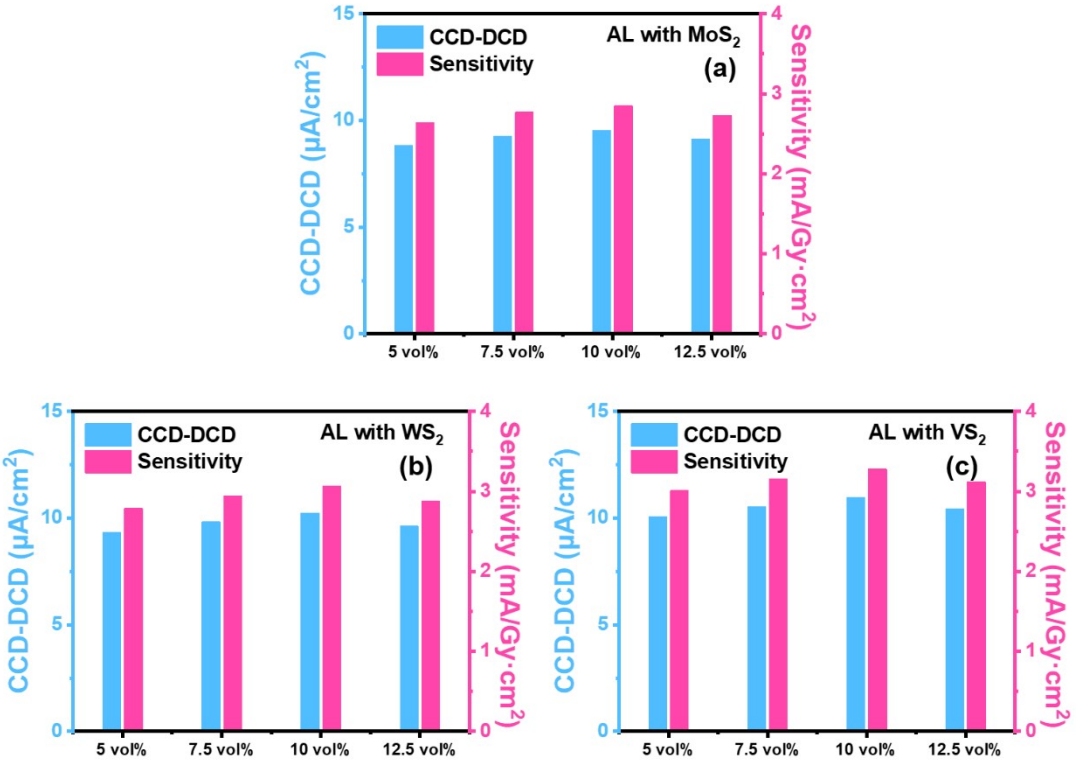

Figure S17. X-ray detector responses with different amount of (a) MoS_2, (b) WS_2 and (c) VS_2 doped $Cs_{0.1}MA_{0.9}PbI_3$ perovskite layer.

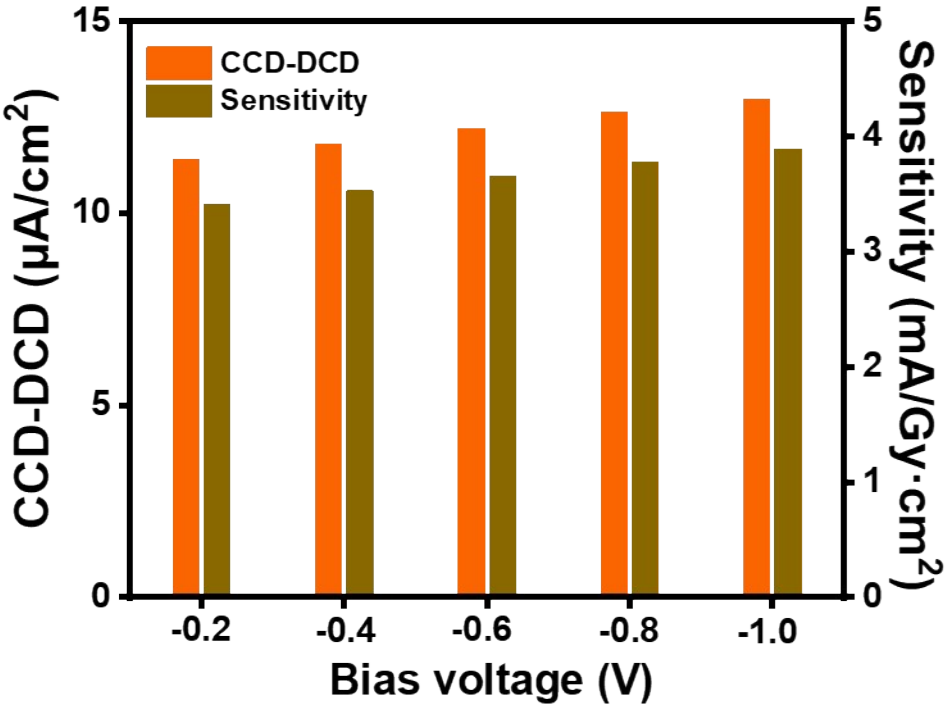

Figure S18. CCD-DCD and sensitivity variations of X-ray detectors prepared using $Cs_{0.1}MA_{0.9}PbI_3$ active layer doped with VW2 VS_2–WS_2 hybrids (10 vol.%) at different applied voltages.

Table S1. Device performance of various perovskite-based photodetectors

Device module	Responsivity	Rise/fall time	Ref.
$Cs_{0.1}MA_{0.9}PbI_3$-VS_2-WS_2 VW2	**73.1 A/W**	**4 / 3 ms**	**This work**
$Cs_{0.1}MA_{0.9}PbI_3$-VS_2-MoS_2 VM2	**22.5 A/W**	**7 / 6 ms**	
$MAPbI_3$	6.1 A/W	-	1
$CsPbBr_3$ QDs/V-MoS_2/Si	0.975 A/W	6.8/6.7 ms	2
$MAPbI_3$ film/graphene	180 A/W	0.087/0.54 s	3
WSe_2/$ReSe_2$	0.3 A/W	4.7/4.1 ms	4
$MAPbI_3$ film/InGaZnO	0.025 A/W	40/100 ms	5
ML MoS_2/$(C_6H_5C_2H_4NH_3)_2PbI_4$	16.8 A/W	5100/10 000 ms	6
$MoTe_2$/InSe	0.015 A/W	720/440 ms	7
$CH_3NH_3PbI_3$/WSe_2	110 A/W	2 s	8
$MAPbI_3$-MoS_2 nanoflakes BHJ film/rGO	1.08×10^4 A/W	<0.045/<0.045s	9
$MAPbI_3$ QDs/TiO_2 NTs	1.3 A/W	2000/1000 ms	10
$CH_3NH_3PbI_3$-WS_2 NCs/rGO	678.8	< 60 or 780 ms	11
$MAPbI_3$ film/MoS_2/APTES	2.11×10^4 A/W	6.17/4.5s	12
$CH_3NH_3PbI_3$/MoS_2	0.6 A/W@0V	2.15 s	13
$MAPbI_3$ film/PDPP3T	0.154 A/W	40/140 ms	14
$CH_3NH_3PbI_3$/WS_2	17 A/W	2.7 ms	15
$(C_6H_5C_2H_4NH_3)_2SnI_4$-($(PEA)_2SnI_4$)/semi-CNT hybrid	6.3×10^4 A/W	825/440 ms	16
$CH_3NH_3PbI_3$/BP/MoS_2	11 A/W	150/240 μs	17
$MAPbI_3$ film/MoS_2	1.1 A/W	-	18
$CsPbI_{3-x}Br_x$ QDs/MoS_2	7.7×10^4 A/W	0.59/0.32	19
Cs-doped $FAPbI_3$/$PdSe_2$	313×10^{-3}	3.5/4 μs	20
Graphene/$(PEA)_2SnI_4$/MoS_2/graphene	0.121 at 0V	34 ms	21
Graphene/$CH_3NH_3PbI_3$/WSe_2/graphene	950@1V A/W	22 ms	22
$FA_{0.85}Cs_{0.15}PbI_3$/$PtSe_2$	0.1@1V A/W	78 ns	23
Triple cation perovskites/MoS_2	342 A/W	27/21 ms	24
$FA_{1-x}Cs_xPbI_3$/$PtSe_2$	313 m A/W	3.5/4 μs	20
$FA_{0.85}Cs_{0.15}PbI_3$/DNTT hybrid	778 A/W	1.1/2.0 ms	25
$Cs_2AgBiBr_6$/SnO_2	0.11 A/W		26
MXene nanoparticles (MNPs)/MoS_2	20.67 A/W	4.62/8.48s	27
$(CH_3NH_3)_3Bi_2Br_9$/MoS_2	112 A/W	0.3/0.3 ms	28

Table S2. Rise and decay time of photodetector for pure and MoX_2 doped perovskite active layer

Mode	**PVK**	**PVK-MoS_2**	**PVK-WS_2**	**PVK-VS_2**	**PVK-VM2**	**PVK-VW2**
Rise Time (ms)	20	15	11	12	7	4
Decay Time (ms)	19	15	11	11	6	3

References

1. N. Cho, F. Li, B. Turedi, L. Sinatra, S. P. Sarmah, M. R. Parida, M. I. Saidaminov, B. Murali, V. M. Burlakov and A. Goriely, *Nature communications*, 2016, **7**, 1-11.
2. L. Guo, Y. Gu, Z. Yang, S. Tian, X. San, J. Liu, L. Gao, S. Qiao and S. Wang, *Advanced Materials Interfaces*, 2021, **8**, 2002231.
3. Y. Lee, J. Kwon, E. Hwang, C. H. Ra, W. J. Yoo, J. H. Ahn, J. H. Park and J. H. Cho, *Advanced materials*, 2015, **27**, 41-46.
4. X. Tian and Y. Liu, *Journal of Semiconductors*, 2021, **42**, 032001.
5. X. Xu, L. Yan, T. Zou, R. Qiu, C. Liu, Q. Dai, J. Chen, S. Zhang and H. Zhou, *ACS applied materials & interfaces*, 2018, **10**, 44144-44151.
6. H. Wang, X. Wang, Y. Chen, S. Zhang, W. Jiang, X. Zhang, J. Qin, J. Wang, X. Li and Y. Pan, *Advanced Optical Materials*, 2020, **8**, 1901402.
7. Y. Sun, W. Gao, X. Li, C. Xia, H. Chen, L. Zhang, D. Luo, W. Fan, N. Huo and J. Li, *Journal of Materials Chemistry C*, 2021, **9**, 10372-10380.
8. J. Lu, A. Carvalho, H. Liu, S. X. Lim, A. H. Castro Neto and C. H. Sow, *Angewandte Chemie*, 2016, **128**, 12124-12128.
9. Z. Y. Peng, J. L. Xu, J. Y. Zhang, X. Gao and S. D. Wang, *Advanced Materials Interfaces*, 2018, **5**, 1800505.
10. Z. Zheng, F. Zhuge, Y. Wang, J. Zhang, L. Gan, X. Zhou, H. Li and T. Zhai, *Advanced Functional Materials*, 2017, **27**, 1703115.
11. D.-D. Zhang and R.-M. Yu, *Frontiers in chemistry*, 2019, **7**, 257.
12. D. H. Kang, S. R. Pae, J. Shim, G. Yoo, J. Jeon, J. W. Leem, J. S. Yu, S. Lee, B. Shin and J. H. Park, *Advanced Materials*, 2016, **28**, 7799-7806.
13. F. Bai, J. Qi, F. Li, Y. Fang, W. Han, H. Wu and Y. Zhang, *Advanced Materials Interfaces*, 2018, **5**, 1701275.
14. S. Chen, C. Teng, M. Zhang, Y. Li, D. Xie and G. Shi, *Advanced Materials*, 2016, **28**, 5969-5974.
15. C. Ma, Y. Shi, W. Hu, M. H. Chiu, Z. Liu, A. Bera, F. Li, H. Wang, L. J. Li and T. Wu, *Advanced Materials*, 2016, **28**, 3683-3689.
16. H. Zhu, A. Liu, H. L. Luque, H. Sun, D. Ji and Y.-Y. Noh, *ACS nano*, 2019, **13**, 3971-3981.
17. L. Wang, X. Zou, J. Lin, J. Jiang, Y. Liu, X. Liu, X. Zhao, Y. F. Liu, J. C. Ho and L. Liao,

ACS nano, 2019, **13**, 4804-4813.

18. Y. Park, S. Lee, H. J. Park, H. W. Baac, G. Yoo and J. Heo, *Journal of Nanoscience and Nanotechnology*, 2016, **16**, 11722-11726.
19. H. Wu, H. Si, Z. Zhang, Z. Kang, P. Wu, L. Zhou, S. Zhang, Z. Zhang, Q. Liao and Y. Zhang, *Advanced Science*, 2018, **5**, 1801219.
20. L. H. Zeng, Q. M. Chen, Z. X. Zhang, D. Wu, H. Yuan, Y. Y. Li, W. Qarony, S. P. Lau, L. B. Luo and Y. H. Tsang, *Advanced Science*, 2019, **6**, 1901134.
21. C. Fang, H. Wang, Z. Shen, H. Shen, S. Wang, J. Ma, J. Wang, H. Luo and D. Li, *ACS applied materials & interfaces*, 2019, **11**, 8419-8427.
22. H.-C. Cheng, G. Wang, D. Li, Q. He, A. Yin, Y. Liu, H. Wu, M. Ding, Y. Huang and X. Duan, *Nano letters*, 2016, **16**, 367-373.
23. Z.-X. Zhang, L.-H. Zeng, X.-W. Tong, Y. Gao, C. Xie, Y. H. Tsang, L.-B. Luo and Y.-C. Wu, *The journal of physical chemistry letters*, 2018, **9**, 1185-1194.
24. B. Sun, S. Xi, Z. Liu, X. Liu, Z. Wang, X. Tan, T. Shi, J. Zhou and G. Liao, *Applied Surface Science*, 2019, **493**, 389-395.
25. L. B. Luo, G. A. Wu, Y. Gao, L. Liang, C. Xie, Z. X. Zhang, X. W. Tong, T. Wang and F. X. Liang, *Advanced Optical Materials*, 2019, **7**, 1900272.
26. C. Wu, B. Du, W. Luo, Y. Liu, T. Li, D. Wang, X. Guo, H. Ting, Z. Fang and S. Wang, *Advanced Optical Materials*, 2018, **6**, 1800811.
27. J. Zou, Y. Huang, W. Wang, C. Li, S. Wei, H. Liu, L. Luo, W. Du, K. Shen and A. Ren, *ACS Applied Materials & Interfaces*, 2022, **14**, 8243-8250.
28. J. He, Y. Yang, Y. He, C. Ge, Y. Zhao, L. Gao and J. Tang, *ACS Photonics*, 2018, **5**, 1877-1884.